Review

# Peptide antibiotics in action: Investigation of polypeptide chains in insoluble environments by rotational-echo double resonance

Orsolya Toke [a], Lynette Cegelski [b], Jacob Schaefer [c],*

[a] Institute for Structural Chemistry, Chemical Research Center of the Hungarian Academy of Sciences, Pusztaszeri út 59-67, H-1025 Budapest, Hungary
[b] Department of Molecular Microbiology, Washington University School of Medicine, 660 S. Euclid Ave., St. Louis, MO 63110, USA
[c] Department of Chemistry, Washington University, One Brookings Drive, St. Louis, MO 63130, USA

## Abstract

Rotational-echo double resonance (REDOR) is a solid-state NMR technique that has the capability of providing intra- and intermolecular distance and orientational restraints in non-crystallizable, poorly soluble heterogeneous molecular systems such as cell membranes and cell walls. In this review, we will present two applications of REDOR: the investigation of a magainin-related antimicrobial peptide in lipid bilayers and the study of a vancomycin-like glycopeptide in the cell walls of *Staphylococcus aureus*.
© 2006 Elsevier B.V. All rights reserved.

*Keywords:* Host-defense peptides; Ion-channels; Membrane pores; Vancomycin; Oritavancin; Cell wall; Solid-state NMR; Dipolar recoupling

## Contents

## 1. Introduction

In addition to fluorescence spectroscopy, neutron diffraction, and a number of other techniques, solid-state NMR has proven to be a powerful technique to gain insight into the modes of action of peptide antibiotics [1,2]. The incorporation of site-specific $^{13}$C, $^{15}$N, $^{2}$H, and $^{19}$F labels into the amino acid sequence provides a way to monitor the secondary structure, location, and aggregation properties of peptide chains *within* lipid bilayers and cell walls, as well as to characterize their structural and dynamic effects on their surroundings (e.g., lipid order in a membrane).

After a brief introduction to solid-state NMR, we will describe two applications of rotational-echo double resonance (REDOR), a solid-state NMR technique for the measurement of weak heteronuclear dipolar couplings [3–5], in our investigation of peptide antibiotics. In one example, the investigation of K3 (KIAGKIAKIAGKIAKIAGKIA), a synthetic analogue [6] of the *Xenopus* peptide PGLa [7], will be presented. This peptide exhibits higher antimicrobial activity than any of the native *Xenopus* peptides (including magainins [8–10]), while maintaining low hemolytic activity at its antimicrobial concentration and had been under clinical trial for the treatment of diabetic foot ulcers. In another example, we will summarize the results of our experiments on [$^{19}$F]oritavancin (Eli Lilly compound LY329332), a vancomycin analogue of improved activity.

## 2. High-resolution NMR in the solid state

### 2.1. Lineshape-dominating interactions in solid-state NMR

In addition to the external static ($B_o$) and alternating ($B_{rf}$) magnetic fields, the two most relevant interactions for an isolated pair of spin-1/2 nuclei (e.g., $^{13}$C, $^{15}$N, $^{31}$P, $^{19}$F) in the solid state are the chemical shift anisotropy (CSA) and the dipolar coupling. For nuclei with spin quantum number larger than 1/2 (e.g., $^{2}$H), there is an additional interaction, the quadrupolar coupling. The energy of the spin system – referred to as the nuclear spin Hamiltonian – can be calculated as the sum of the individual spin interactions [11–14]. While the external fields provide the basis for magnetic resonance, the three other terms contribute to the local fields that influence the nuclei and that carry important structural information.

All three of these interactions depend upon the orientation of the molecular segment with respect to the external magnetic field. For instance, the chemical shift anisotropy originates from the fact that the electron cloud around the nucleus generates an additional local magnetic field, which 'shields' the nucleus from the external magnetic field. As the shape of the electron cloud depends upon the bonding network, the shift of the precession frequency from that of the unshielded nucleus will be a function of the polar and azimuthal angles that define the orientation of the molecular segment in the laboratory frame (an *xyz* coordinate system whose z-axis is pointing parallel to $B_o$). Similarly, for the dipolar and quadrupolar couplings, the energy of the interaction depends upon the relative orientation of the molecular segment with respect to $B_o$. Both of these interactions will give rise to a splitting of the resonance signal just as J couplings cause splittings in solution NMR. In addition to the orientation dependence discussed above, the magnetic energy that two interacting nuclei acquire in each others field is also dependent upon the distance between the two spins ($1/r^3$), making the dipolar interaction highly valuable in structural studies.

In solution state, fast isotropic tumbling of the molecules averages out the orientation dependent terms, leaving only the isotropic chemical shift and scalar coupling in the NMR spectrum. In molecular systems that exhibit no or only restricted motion on the time-scale of anisotropic spin-interactions (such as membrane proteins in lipid bilayers), these spin-interactions dominate the lineshape. In systems in which all possible molecular orientations are present with equal probabilities, the stationary NMR experiment results in an inhomogeneously broadened powder pattern. Although a tremendous amount of structural information is encoded in this pattern, for a multispin system, most of it is completely hidden in the broadened lineshape.

### 2.2. Line-narrowing techniques in solid-state NMR

There are three main approaches for obtaining high-resolution spectra in solid-state NMR. One approach relies upon orienting the sample, either mechanically [15] or with an external magnetic field [16,17]. In this case, the uniaxial orientation provides a mechanism for line narrowing, yet the structural information inherent in the anisotropic spin interactions is retained.

Another approach originally developed for $^{1}$H NMR is 'multiple pulse line-narrowing' [18–20] which involves the rotation of nuclear spins by radiofrequency (RF) pulses in such a way that over a cycle the average homonuclear dipolar interaction vanishes. This methodology later on provided the basis for the development of the so-called separated local field (SLF) experiments [21,22] in which the anisotropic chemical shift and heteronuclear dipolar coupling interactions are sorted into different spectral dimensions. Over the last decade, SLF experiments, such as PISEMA (polarization inversion spin exchange at the magic angle) [23] have proven to be highly powerful techniques in the study of aligned membrane samples.

Finally, the third approach to achieve line-narrowing in solid-state NMR is magic angle spinning (MAS) [24,25]. MAS increases spectral resolution by mechanically rotating the sample about an axis aligned at a specific angle (54.7°, the magic angle) relative to the external magnetic field. During spinning, the spatial orientation of the nuclei is constantly changing, making their spin interactions and resonance frequencies time dependent. With a handful of trigonometric manipulations, it can be shown that ultra-fast MAS results in an averaging of the CSA to the isotropic chemical shift. This means that the NMR signal will be fully recovered after each rotor period yielding a rotational-echo train. Fourier transformation of the echo train results in a spectrum consisting of, in general, a centerband at the isotropic chemical shift frequency and sidebands separated by the spinning frequency. The sideband intensities depend upon the strength of the internal interactions and decrease with increasing spinning speed.

Similarly to the CSA interaction, it can be shown that the alignment of the rotor axis at the magic angle with respect to $B_o$ has an averaging effect on the dipolar coupling as well. In particular, when the spinning speed exceeds the strength of the dipolar interaction (which in a multispin system is most often needed to avoid the overlap of spinning sidebands), the latter will be averaged to zero. This means that fast spinning results not only in simplification of the spectrum and increased resolution, but also in the loss of important structural information.
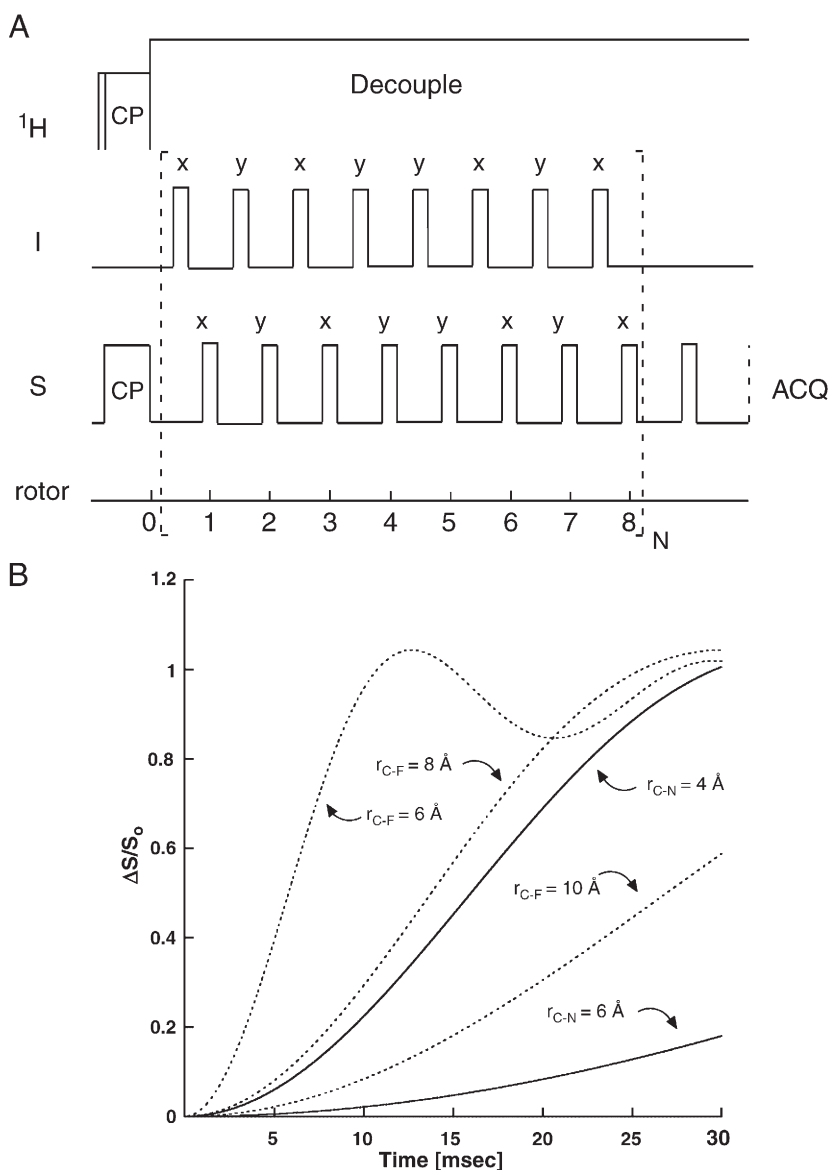


Fig. 1. (A) REDOR pulse sequence using the XY8 pulse cycling scheme [29] to eliminate the effects of offsets and pulse imperfections. After cross-polarization from the abundant protons, a π pulse is applied in the middle of each rotor cycle on the I spin and at the end of each rotor period on the S spin. Application of the two equally spaced π pulses per rotor period results in the dephasing of the transverse S magnetization. Signal acquisition begins two rotor cycles after the completion of 8N rotor cycles of dephasing. The effect of protons is removed by high-power decoupling during the evolution and acquisition periods. The full echo spectrum ($S_o$) is obtained under the same conditions, without the application of the dephasing π pulses on the I channel. (B) REDOR dephasing curves for isolated $^{13}C-^{15}N$ (———) and $^{13}C-^{19}F$ (······) spin pairs at different distances. The initial slope depends on the gyromagnetic ratios of the coupled nuclei and the distance between them. For a given spin pair the slope is determined solely by the internuclear distance.

## 2.3. Dipolar recoupling under magic angle spinning

Since the introduction of MAS, numerous NMR techniques have been designed to reintroduce homo- and heteronuclear dipolar couplings under MAS conditions [26–28]. Dipolar interactions can be recoupled by either carefully selecting the rotational frequency to match a nuclear energy level or by the application of rotor-synchronized radiofrequency pulse trains.

For instance, a typical pulse sequence for an I–S rare-spin pair in a REDOR experiment is shown in Fig. 1A [3,4,29]. In this case, S is the observed spin and I is the so-called dephasing spin. The experiment starts with the establishment of transverse magnetization of spin S by cross-polarization transfer from the abundant proton reservoir, followed by a dipolar evolution period that contains two sets of rotor-synchronized interleaved pulse trains. One set consists of I-spin $\pi$ pulses in the middle of each rotor period, and the other set consists of S-spin $\pi$ pulses at the end of each rotor period. Two spectra are collected: one with the pulses on the I channel to produce the dephased spectrum ($S$) and another one without the dephasing pulses to produce the full echo signal ($S_o$). The difference between the two spectra ($\Delta S = S_o - S$) depends on the I–S dipolar coupling and hence on the I–S internuclear distance (Fig. 1B).

REDOR measures internuclear distances up to 6–20 Å, depending on the gyromagnetic ratios and the sensitivities of the nuclei involved. Two advantages of REDOR are that it does not depend on the chemical shift tensors of the coupled nuclei and that it does not require the resolution of the I–S dipolar coupling in the chemical shift dimension. A complication is that natural-abundance contributions must be taken into account. In some cases, comparison with an unlabeled sample is necessary which can be elaborate and time consuming. To overcome these difficulties, a pulse sequence called transferred echo double resonance (TEDOR) [30] was developed in which the dipolar-coupled spins can be selected from the background of uncoupled spins. TEDOR can be used alone or in combination with a REDOR sequence. For example, an S–X dipolar coupling in a specific I–S–X labeled triplet can be measured by first selecting the S spin by a coherence transfer from I. The TEDOR selection is followed by the REDOR part in which the dipolar coupling between spins S and X is determined.

In addition to REDOR and TEDOR, there are a number of other techniques to reintroduce the dipolar coupling into MAS spectra. The list includes R$^2$ [31], DRAMA [32], SEDRA [33], CEDRA [34], DRAWS [35], CROWN [36], HORROR [37], BABA [38], C7 [39], RFDR [40], MELODRAMA [41], R$^3$ [42, 43]. These techniques are discussed in detail in several excellent reviews [26,28,44].

## 3. Applications of REDOR in the study of antimicrobial peptides

### 3.1. Antimicrobial peptides: new candidates for antibiotics

Over the past several decades, the search for new drugs and target sites has prompted an interest in a group of short, 10– 40 residue polypeptides, called antimicrobial peptides (AMPs). As part of the innate defense system, AMPs provide protection against a wide variety of microorganisms in both vertebrates and invertebrates [45–51]. Their killing mechanism is thought to involve ion channel or pore formation and the dissipation of the electrochemical gradient across the bacterial cell membrane. In some cases, there are indications that killing may require a more robust disintegration of the pathogenic cell membrane [52,53]. At a time of increasing bacterial resistance, the physical nature of their killing mechanism makes them one of the most intriguing and promising candidates for novel antibiotics. Understanding their mode of action at the molecular level is crucial for AMP-based drug development. Solid-state NMR offers an opportunity to investigate the various properties of polypeptide chains in phospholipid bilayers, which for most antimicrobial peptides resembles their physiological site of action: the bacterial cell membrane. With the employment of site-specific labeling, information on peptide conformation, peptide–peptide, as well as peptide–lipid interactions can be obtained at a single residue level.

Currently, there are three main models of peptide-induced pore formation in lipid bilayers (Fig. 2): (1) In the conventional barrel-stave model [54,55], peptide chains are oriented perpendicular to the membrane surface. While their hydrophobic face interacts with the non-polar lipid acyl chains, their hydrophilic face forms the interior of a barrel-stave pore made of several peptides. (2) In the 'carpet-mechanism' [56–58], reorientation of the peptide chains is hindered by strong electrostatic interactions between the positively charged peptide sidechains and the often negatively charged lipid headgroups. Accumulation of peptide chains on the membrane surface causes tension between the two leaflets of the bilayer that leads to disintegration/rupture of the membrane. (3) In the 'toroid (or wormhole) model' [10,59], peptide chains and lipid headgroups together line the wall of the pore. Although the peptide chains are oriented perpendicular to the membrane surface, due to the reorientation of the lipid molecules, they remain at the hydrophobic/hydrophilic interface.

We should note that, recently, significantly different structural and dynamic characteristics have been obtained for RTD, the mammalian cyclic θ-defensin [60] by static $^2$H and $^{31}$P NMR experiments of oriented phosphatidylcholine bilayers [61], which may be an indication of the existence of a fourth possible mechanism of pore formation.

To distinguish between the various pore models, our approach has been to introduce specific $^{13}$C, $^{15}$N, and $^{19}$F labels into K3 so that (i) isotropic chemical shifts reveal its local secondary structure at the middle and near both ends of the peptide chain; (ii) intermolecular heteronuclear dipolar couplings reveal chain aggregation and orientation; (iii) the proximities of labels in the peptide chains to $^{31}$P and $^{19}$F incorporated in the lipids establish the positioning of K3 relative to the phospholipid headgroups and tails; and (iv) headgroup–lipid tail contacts provide us with information on the effect of K3 on lipid chain ordering in the bilayer.
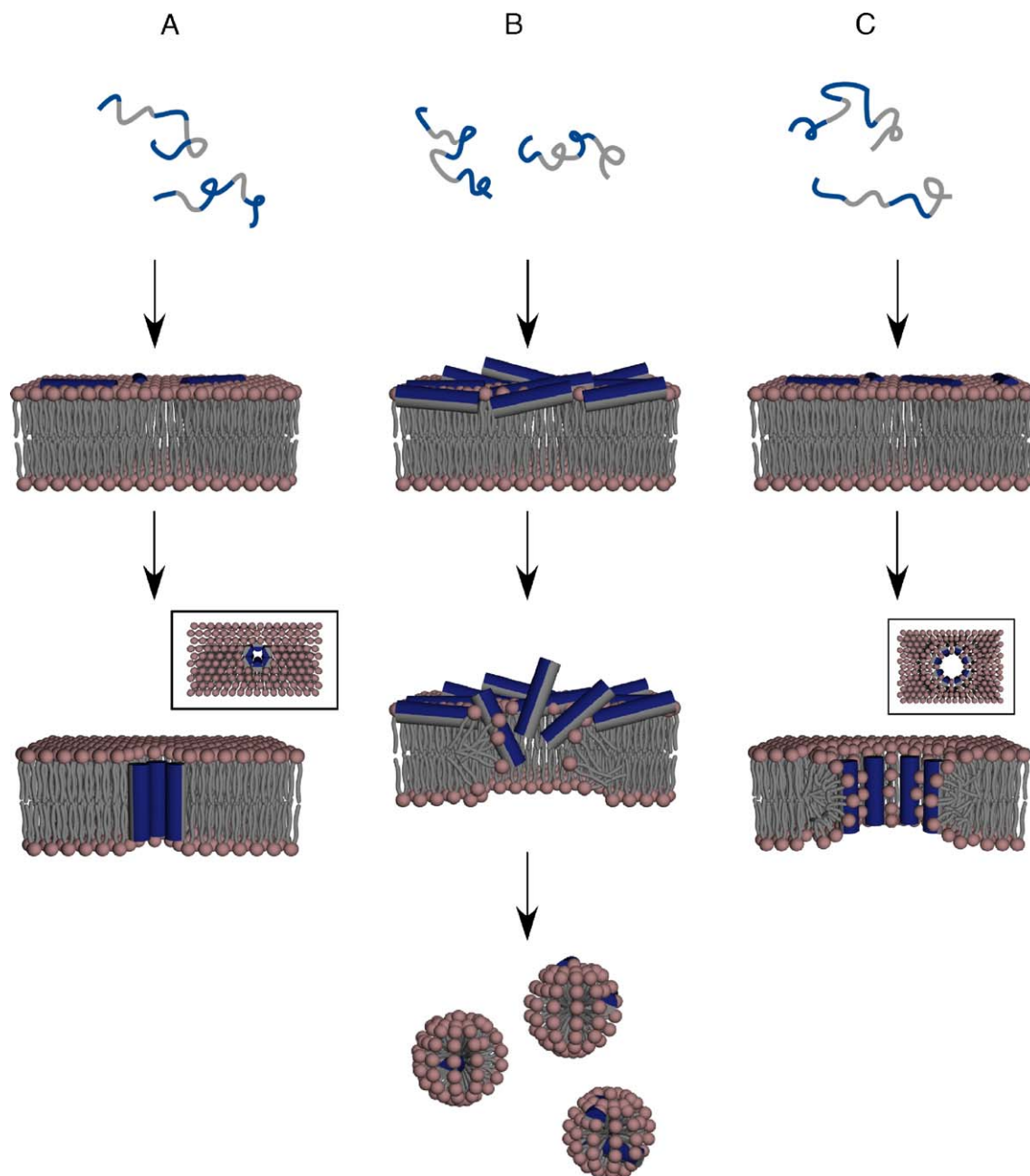
Fig. 2. Cartoons illustrating the permeabilization mechanisms of alpha-helical antimicrobial peptides [51]: (A) barrel-stave, (B) carpet (detergent-like), and (C) toroidal (wormhole). The hydrophilic and hydrophobic faces of the peptides (shown as cylinders) are colored in blue and gray, respectively. The top-views for the barrel-stave and the toroidal pore models are shown in boxes.

## 3.2. Secondary structure

The relationship between backbone chemical shifts and protein secondary structure has long been recognized. In solution NMR, the chemical shift index (CSI) [62,63] and the TALOS [64] algorithms were developed in the 1990s and are widely used methods for secondary structure determination. Ab initio calculations of shielding surfaces and isotropic chemical shifts for the amide nitrogen and various carbon atoms in the 20 common amino acids as a function of the backbone torsion angles are used to confirm and refine the empirical correlations [65–68].

Similarly to the observations in solution NMR, one approach in obtaining information on peptide secondary structure by solid-state NMR relies on the fact that alpha-helical methyl and carbonyl carbon chemical shifts of peptides can differ from those in beta-sheet conformation by up to 8 ppm [69]. Thus, carefully positioned, non-perturbing $^{13}C$-labels in the sequence can provide a direct answer. To overcome the difficulty posed by the large lipid background in the case of membrane-embedded antimicrobial peptides, dipolar-recoupling techniques can be used under MAS conditions as spectral editing tools. For instance, in the study of K3, we incorporated $^{13}C$ and $^{15}N$ labels at the beginning, middle and end of the peptide chain
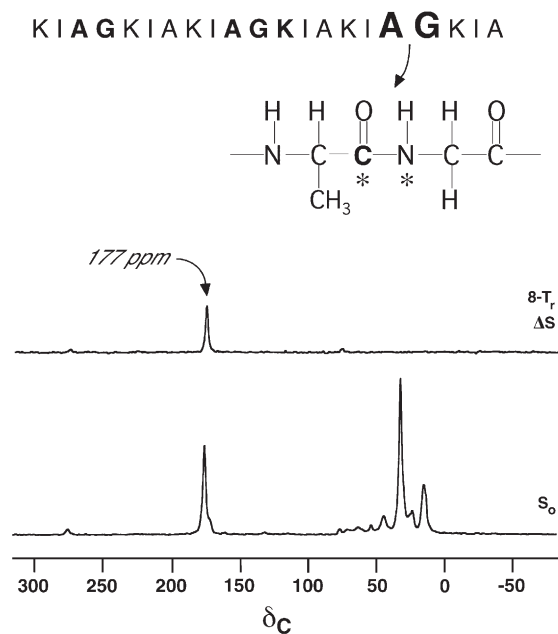
Fig. 3. 50.3-MHz REDOR $^{13}$C{$^{15}$N} NMR spectra of [3-$^{13}$C]Ala$_3$–[$^{15}$N]Gly$_4$–[1-$^{13}$C]Ala$_{10}$–[2-$^{13}$C]Gly$_{11}$–[6-$^{15}$N]Lys$_{12}$–[1-$^{13}$C]Ala$_{17}$–[$^{15}$N]Gly$_{18}$–K3–NH$_2$ incorporated into MLVs of DPPG and DPPC (1:1) at a lipid-to-peptide molar ratio of 10, after 8 rotor cycles of dipolar evolution with MAS at 5000 Hz [70]. The full-echo spectrum ($S_o$) is shown at the bottom of the figure and the REDOR difference spectrum ($\Delta S$, the difference between the $^{13}$C echo intensities observed without and with $^{15}$N dephasing pulses) at the top.

[70]. The resonance frequency of each $^{13}$C label was individually selected by a specific recoupling scheme, making it possible to probe the secondary structure at various positions in the sequence. For example, a completely unambiguous determination of the carbonyl-carbon resonance frequency of [1-$^{13}$C]Ala$_{17}$ was made using a $^{13}$C{$^{15}$N} REDOR experiment with a dipolar evolution time of 1.6 ms (8 rotor cycles with MAS at 5 kHz) (Fig. 3). In this situation, only $^{13}$C-s with a strong, one-bond $^{13}$C–$^{15}$N dipolar coupling appear in the REDOR difference spectrum, and the only carbonyl $^{13}$C in the labeled sample that fits this description is the carbonyl carbon of Ala$_{17}$. This demonstrates the utility of REDOR as a spectral editing tool. Even if the lipid (upfield shoulder of the peak at 177 ppm) and Ala$_{17}$ carbonyl peaks were completely unresolvable, there would be no interference from the lipid signal in the difference spectrum.

The resonance frequencies of the $^{13}$C methyl carbon of Ala$_3$ and the $^{13}$C carbonyl carbon of Ala$_{10}$ in K3 were determined in a similar manner, leading to the conclusion that the entire K3 chain was in an alpha-helical conformation in the lipid bilayer. A similar $^{13}$C{$^{15}$N} REDOR experiment was used to establish the secondary structure of the C-terminal region of pardaxin, an antimicrobial peptide from the Red Sea Moses sole fish *Pardachirus marmoratus*, in various lipid bilayers [71].

A different method for the determination of peptide conformation is distance measurement between selectively labeled residues combined with molecular modeling. This can be particularly valuable in obtaining structural restraints in less ordered regions. Also, distance measurements can be used as

independent experiments to confirm the secondary structure information obtained from chemical shifts. For instance, in a study of a magainin 2 analogue, the 4.1 Å distance measured between [1-$^{13}$C]–Ala$_{15}$ and [$^{15}$N]–Ala$_{19}$ by REDOR was only consistent with an alpha-helical conformation and served as an independent piece of evidence in the structure determination [72].

### 3.3. Peptide aggregation

Dipolar recoupling techniques have proven to be highly valuable in the study of peptide aggregation. For example, a $^{13}$C{$^{19}$F} REDOR experiment in a selectively labeled sample can provide intermolecular distance restraints up to 12 Å. This is well exemplified by the investigation of K3 in phospholipid model membranes [73] (Fig. 4). The full-echo $^{13}$C spectrum ($S_o$) of an equimolar mixture of [1-$^{13}$C]–Ala$_{10}$–[$^{15}$N]–Gly$_{11}$–K3 and [3-$^{19}$F]–Ala$_{10}$–K3 in multilamellar vesicles of DPPC and DPPG is shown in the bottom of the figure. Besides the labeled carbonyl position, this spectrum has contributions from natural abundance lipid and peptide background. The $^{13}$C carbonyl of Ala$_{10}$ can be selected by the strong one-bond $^{13}$C–$^{15}$N dipolar coupling via a short, 4-rotor cycle TEDOR coherence transfer. The TEDOR sequence is followed by 48 additional rotor cycles first in the absence (TEDOR-$S_o$, middle) then in the presence of $^{19}$F dephasing pulses. The appearance of a sizeable $^{15}$N→$^{13}$C{$^{19}$F} TEDOR-REDOR difference signal ($\Delta S$, top) is
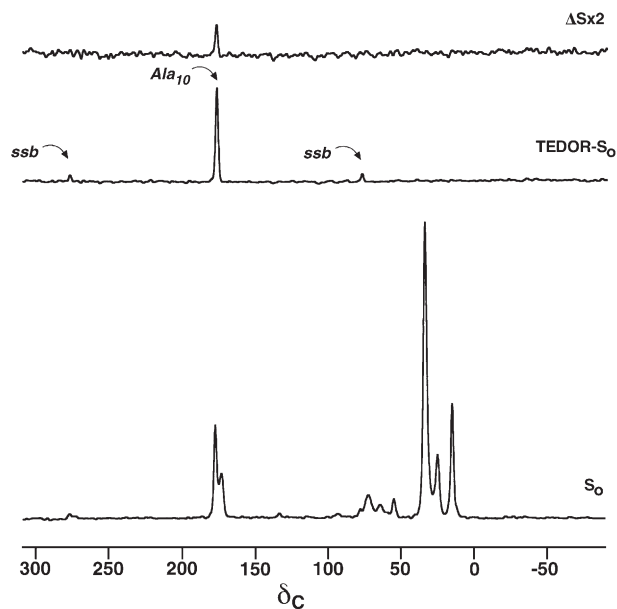


Fig. 4. 50.3 MHz $^{15}$N→$^{13}$C{$^{19}$F} TEDOR-REDOR NMR spectra of a fifty–fifty mixture of [1-$^{13}$C]Ala$_{10}$–[$^{15}$N]Gly$_{11}$–K3–NH$_2$ and [2-$^2$H, 3-$^{19}$F]Ala$_{10}$–K3–NH$_2$ incorporated into synthetic MLVs of DPPG-DPPC (1:1) at a lipid-to-peptide molar ratio of 20, after 48 rotor cycles of dipolar evolution with magic-angle spinning at 5000 Hz [73]. The 48-T$_r$ full-echo spectrum ($S_o$) is shown at the bottom of the figure. The middle spectrum resulted from a 4-T$_r$ $^{15}$N→$^{13}$C TEDOR coherence transfer followed by 48 additional rotor cycles with high power proton decoupling. The 48-T$_r$ REDOR $\Delta S$ spectrum (where $\Delta S$ is the difference between the $^{13}$C echo intensities observed without and with $^{19}$F dephasing pulses) of the TEDOR selected signal is shown at the top of the figure.

Fig. 5. 50.3-MHz $^{13}C\{^{19}F\}$ REDOR dephasing ($\Delta S/S_o$) curves of a fifty–fifty mixture of $[1\text{-}^{13}C]Ala_{10}$–$[^{15}N]Gly_{11}$–K3–NH$_2$ and $[2\text{-}^2H, 3\tex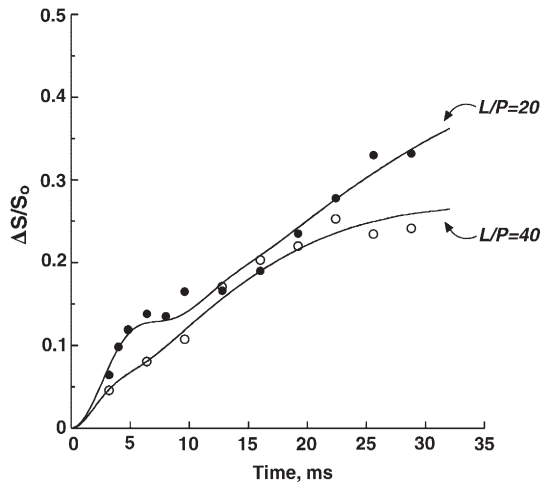t{-}^{19}F]Ala_{10}$–K3–NH$_2$, incorporated into synthetic MLVs of DPPG-DPPC (1:1) at a lipid-to-peptide molar ratio (L/P) of 20 (closed circles) and 40 (open circles) [73]. Both samples were lyophilized in a protecting sugar matrix. The solid lines are simulated dephasing curves that correspond to a bimodal distribution of C–F distances with the following parameters: i) L/P = 20, mean internuclear $^{13}C$–$^{19}F$ separations of 4.6 Å and 9.6 Å with widths of 0.7 Å and 3 Å, respectively; ii) L/P = 40, mean internuclear $^{13}C$–$^{19}F$ separations of 4.3 Å and 8.1 Å with widths of 1.0 Å and 3.2 Å, respectively. At L/P = 40, the population with the smaller mean and narrower distribution width decreases.

a manifestation of the intermolecular $[1\text{-}^{13}C]$–Ala$_{10}$–$[3\text{-}^{19}F]$–Ala$_{10}$ dipolar coupling and unambiguously proves the proximity of peptide chains in the membrane.

The measurement of $\Delta S/S_o$ ratios at different dephasing times (Fig. 5) allows the determination of the separation between peptide chains, as well as the estimation of the fraction of peptide molecules, which are near another chain. For K3, at a lipid-to-peptide molar ratio close to that of the therapeutic concentration, least-square analysis of the REDOR curve showed a bimodal distribution of internuclear $[1\text{-}^{13}C]$–Ala$_{10}$–$[3\text{-}^{19}F]$–Ala$_{10}$ distances: a narrow distribution centered at 4.6 Å and a broad distribution centered at 9.6 Å. (The existence of two distinct populations of $^{13}C$–$^{19}F$ distances is also apparent from a visual inspection of the REDOR curve, i.e., the 'bump' at short dephasing times.) The narrow distribution at short interchain distances suggested specific interactions between K3 chains (dimerization has later on been confirmed by additional experiments), whereas the broad distribution at longer distances reflected less specific interactions between the peptide chains, possibly a loose aggregate of peptide monomers and dimers in a membrane pore. The population of closely-packed K3 dimers has increased by almost three-fold between L/P = 40 and L/P = 20. The concentration dependent dimerization of K3 chains was consistent with the sigmoidal nature of binding isotherms of similar, magainin-like AMPs to negatively charged lipid vesicles [9,74,75].

Once aggregation is established, distance measurements can provide information on the relative orientation of peptide chains within the aggregate. For instance, changing the position of the $^{13}C$ and $^{19}F$ labels in K3, REDOR revealed a head-to-head arrangement of helices within the dimer [73]. Also, as spinning

sidebands in MAS experiments (e.g., the small peaks around 75 and 275 ppm in the TEDOR-$S_o$ spectrum in the middle of Fig. 4) are composed of their own CSA-weighted distributions of CSA-tensor orientations, differences in sideband dephasing rates are indications of a preferred relative orientation between the CSA and dipolar tensors. This can be exploited for obtaining orientational restraints in REDOR experiments [76], which in combination with the interchain distance information and molecular modeling can lead to the determination of the relative orientation of two interacting helices in membrane bilayers. For K3, we obtained a dimer structure in which the two helices intersect at a cross-angle of ~20° [73] (Fig. 6). Similar solid-state NMR experiments have been used with great success to determine the directionality of amyloid-forming Aβ peptides [77] and to obtain absolute structural constraints in fibrils [78].

We note that dipolar recoupling experiments can also be used to gain insight into the size and shape of aggregates. For instance, if the peptide chains form trimers or larger aggregates, the distance measurement in a $^{13}C\{^{19}F\}$ REDOR experiment is expected to deviate in a predictable way from that observed for isolated spin pairs [79]. This can be exploited in titration experiments where the ratio of the $^{13}C$, $^{15}N$-labeled peptide to $^{19}F$-labeled peptide is varied. For example, if oligomerization involves the formation of a peptide hexamer, at low isotopic concentrations of the $^{13}C$, $^{15}N$-labeled peptide, each $^{15}N$-selected $^{13}C$ label in the middle of a peptide chain will be surrounded by five $^{19}F$-labeled peptides. In combination with molecular modeling, the positions of all five $^{19}F$ labels might be inferred from REDOR experiments in which the dipolar evolution time is varied.
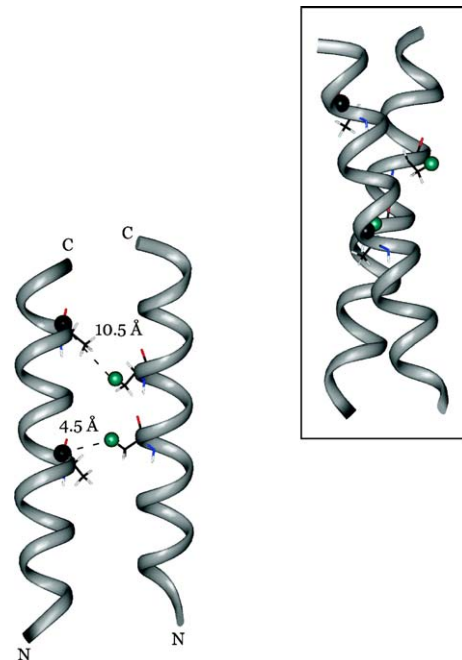


Fig. 6. Cartoon of the dimerized K3 chains obtained from the combination of distance and angular information [73]. After energy minimization, the $[1\text{-}^{13}C]$Ala$_{10}$–$[3\text{-}^{19}F]$Ala$_{10}$ and the $[1\text{-}^{13}C]$Ala$_{17}$–$[3\text{-}^{19}F]$Ala$_{14}$ interchain distances are 4.5 Å and 10.5 Å, respectively. The REDOR determined distances were 4.6 Å and 10.4 Å. The helices interact at an approximate cross-angle of 20° (inset).

### 3.4. Orientation and location of peptide chains within lipid bilayers

The phosphorous atom in phospholipid headgroups (a spin-1/2 isotope of 100% abundance) is a natural spin label that can be exploited in obtaining distance restraints. By incorporating $^{13}C$ or $^{15}N$ labels at various locations in the peptide sequence, $^{13}C\{^{31}P\}$ and $^{15}N\{^{31}P\}$ REDOR experiments can be used to determine their proximity to the lipid headgroups. For instance, the $^{13}C\{^{31}P\}$ REDOR full-echo ($S_o$) and difference ($\Delta S$) spectra of [3-$^{13}C$]Ala$_3$–[$^{15}N$]Gly$_4$–[1-$^{13}C$]Ala$_{10}$–[2-$^{13}C$]Gly$_{11}$–[6-$^{15}N$]Lys$_{12}$–[1-$^{13}C$]Ala$_{17}$–[$^{15}N$]Gly$_{18}$-labeled K3 incorporated into multilamellar vesicles of DPPC/DPPG (1:1) at a lipid-to-peptide molar ratio of 20 is shown in Fig. 7 after 19.2 ms of dipolar evolution time [70]. The sizeable dephasing at 177.2 ppm arises from $^{13}C$ carbonyl labels at Ala$_{10}$ and Ala$_{17}$ (see above on Secondary structure) and indicates the proximity of the peptide chain to the phosphorous headgroups. (The upfield peak at 173.2 ppm in both spectra is from natural abundance $^{13}C$ lipid carbonyls whose dephasing arises mainly from short intramolecular $^{13}C$–$^{31}P$ contacts in the phospholipids with a small intermolecular contribution between neighboring lipid headgroups.) We note that the $^{13}C$ label at Ala$_{17}$ could have also been selected via the [1-$^{13}C$]Ala$_{17}$–[$^{15}N$]Gly$_{18}$ one-bond heteronuclear dipolar coupling preceding the $^{31}P$ dephasing if desired. In addition to the peaks in the carbonyl region, the peak in the $\Delta S$ spectrum at 16.1 ppm can be attributed to the $^{13}C$ methyl label in Ala$_3$ and indicates a contact
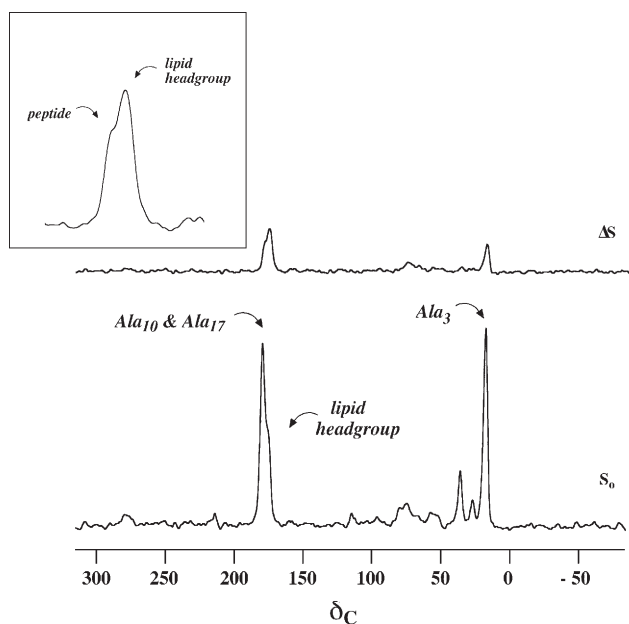


Fig. 7. 50.3-MHz $^{13}C\{^{31}P\}$ REDOR full-echo ($S_o$) and difference ($\Delta S$) spectra of [3-$^{13}C$]Ala$_3$–[$^{15}N$]Gly$_4$–[1-$^{13}C$]Ala$_{10}$–[2-$^{13}C$]Gly$_{11}$–[6-$^{15}N$]Lys$_{12}$–[1-$^{13}C$]Ala$_{17}$–[$^{15}N$]Gly$_{18}$-K3–NH$_2$, incorporated into synthetic MLVs of DPPG-DPPC (1:1) at a lipid-to-peptide molar ratio of 20 after 96 rotor cycles of dipolar evolution with magic-angle spinning at 5000 Hz [70]. The C$_\alpha$ of Gly has a short T$_2$ relaxation and therefore it is not observed in the spectrum after 96 rotor cycles. An expansion of the 175 ppm region of the difference spectrum is shown in the inset.

between the N-terminal region of the peptide and the lipid headgroups.

By monitoring the $^{13}C\{^{31}P\}$ dephasing for the carbonyl carbon at Ala$_{10}$ as a function of dipolar evolution time, we obtained an apparent average C–P distance of 5 Å for K3 at peptide concentrations where pore formation was observed. We should emphasize that since there are multiple phosphorous dephasers whose contributions in this situation are difficult to deconvolute, this is only a qualitative determination of the proximity of Ala$_{10}$ to the lipid headgroups (±1 Å). However, the *extent* of peptide–headgroup contact as a function of peptide concentration became a valuable piece of evidence in the exclusion of the possibility of a barrel-stave pore model [70,73].

To obtain more information on the orientation of K3 in membrane systems, we also carried out static NMR experiments on oriented lipid bilayers. Static NMR experiments are extensively used in the study of AMPs [80–83] and membrane proteins in general and have recently been reviewed in detail [84]. For K3, they showed a reorientation of peptide chains between L/P = 200 and L/P = 20 [73] and provided a crucial piece of evidence in the establishment of the pore model.

### 3.5. The effect of AMPs on lipid order in the bilayer

The analysis of static $^{31}P$ and $^2H$ spectra of phospholipid bilayers containing various amounts of an antimicrobial peptide can reveal important details on how that particular AMP influences the structure and dynamics of lipid bilayers [81,85], including the effect on membrane curvature and phospholipid morphology [82].

As an alternative approach, information on lipid order in the presence and absence of antimicrobial peptides can also be obtained by the characterization of the headgroup–lipid tail contact in the bilayer. This can be done, for instance, by the incorporation of an $^{19}F$ label at low, non-perturbing concentrations into the tail of lipid acyl chains and the employment of a $^{31}P\{^{19}F\}$ REDOR experiment. This is shown in Fig. 8A for MLVs of DPPG/DPPC (2.5 mol% F-lipid included) with and without the incorporation of the synthetic magainin-analogue, K3, as a function of dipolar evolution time [70]. The presence of the peptide results in a larger fraction of lipid headgroups that are in proximity to the lipid tails (higher plateau), and a shorter average P–F distance (larger slope of the $\Delta S/S_o$ curve). In addition, the distribution of P–F distances increases dramatically (Fig. 8B), indicating an increased disorder among the lipid molecules when K3 is present.

### 3.6. Pore model

During the last decade or so, solid-state NMR provided direct structural evidence for several AMPs that enabled the investigators to distinguish between various pore models. The studies usually employ a combination of several different types of NMR experiments (often both static and MAS experiments), each directed at specific aspects of the mode of action of AMPs.

In our investigation of K3, $^{13}C\{^{31}P\}$ REDOR experiments have proven the proximity of the middle of the peptide chains

to the lipid headgroups, excluding the barrel-stave mechanism. At the same time, static NMR experiments on specifically $^{19}$F-labeled K3 in oriented lipid bilayers have shown a change in orientation of the K3 helix relative to the bilayer normal with increasing peptide concentration. This, and the absence of sharp, isotropic peaks from the static $^{31}$P spectra excluded the possibility of micellization and therefore the carpet mechanism. $^{13}$C{$^{19}$F} REDOR experiments on the mixture of specifically $^{13}$C or $^{19}$F labeled peptides have proven the dimerization of K3 chains within the lipid bilayer as well as the existence of a less specific, larger association of
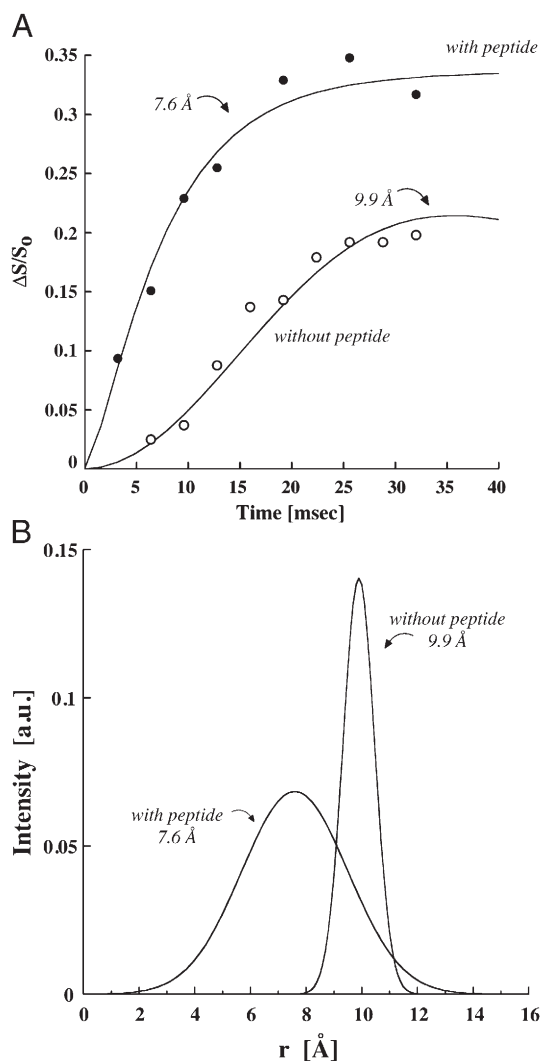


Fig. 9. Cartoons of the K3 pore model: cross section *(top)* and top view *(bottom)* [73]. K3 monomers and dimers are shown in yellow and red, respectively. Lysine side chains are indicated in blue. Peptide chains and lipid headgroups together line the wall of the torus-like pore. A few of kinked lipid chains have $^{19}$F-labeled tails (green) near the phospholipid headgroups.

monomers and dimers interspersed with lipid headgroups [73]. All of these results were consistent with the formation of torus-type pores (Fig. 9) most likely as transient holes in the bilayer before the collapse of the membrane [86].

## 4. Applications of REDOR in the study of glycopeptide antibiotics

### 4.1. Vancomycin resistance

Vancomycin and other closely related glycopeptides inhibit the peptidoglycan biosynthesis of the bacterial cell wall of Gram-positive bacteria [87] (Fig. 10). Cell-wall and septal thinning result from vancomycin treatment [88] because the balance between new cell-wall synthesis at the cell-membrane surface and enzymatic degradation of outer layers (which normally functions to accommodate cell growth and division) is dramatically perturbed. The antibiotics do not penetrate into the cytoplasm of the cell but form complexes with the D-Ala–D-Ala carboxyl termini of peptidoglycan precursors outside the cell membrane [89,90], including lipid II, which is the peptidoglycan repeat unit complexed to a $C_{55}$-lipid transporter. In principle, binding of vancomycin to lipid II could interfere with the activity of transglycosylase and transpeptidase [91–94]. Both are essential for the synthesis of new cell wall. The former extends the glycan chain and the latter cross-links the peptide stems with the subsequent elimination of the terminal D-Ala. Solid-state NMR measurements have been used to measure the production of cross-links and bridge-links in the cell walls of actively dividing *S. aureus*. These experiments showed that transglycosylation is inhibited by vancomycin before any effect on transpeptidation is observed [94].



Fig. 8. 81-MHz $^{31}$P{$^{19}$F} REDOR dephasing ($\Delta S/S_o$) of DPPG/F-DPPG/DPPC/F-DPPC (48.75:1.25:48.75:1.25) MLVs in the presence (closed circles) and in the absence (open circles) of [3-$^{13}$C]Ala$_3$–[$^{15}$N]Gly$_4$–[1-$^{13}$C]Ala$_{10}$–[2-$^{13}$C]Gly$_{11}$–[6-$^{15}$N]Lys$_{12}$–[1-$^{13}$C]Ala$_{17}$–[$^{15}$N]Gly$_{18}$–K3–NH$_2$ at a lipid-to-peptide molar ratio of 20 [70]. Both samples were lyophilized in a protecting sugar matrix. (A) The solid lines drawn through the experimental points are simulated dephasing curves assuming a distribution of isolated $^{31}$P–$^{19}$F spin pairs with a mean internuclear separation of 7.6 Å and a distribution width of 5.4 Å (solid circles), or a mean internuclear separation of 9.9 Å with a distribution width of 1.6 Å (open circles). (B) Distribution of $^{31}$P–$^{19}$F distances in the presence and in the absence of K3 in the bilayer. F-DPPG=1-palmitoyl-2-[16-fluoropalmitoyl]-phosphatidylglycerol; F-DPPC=1-palmitoyl-2-[16-fluoropalmitoyl]-phosphatidylcholine.
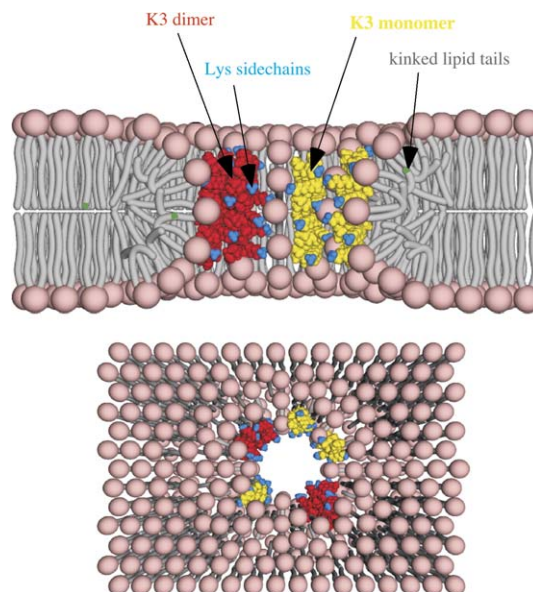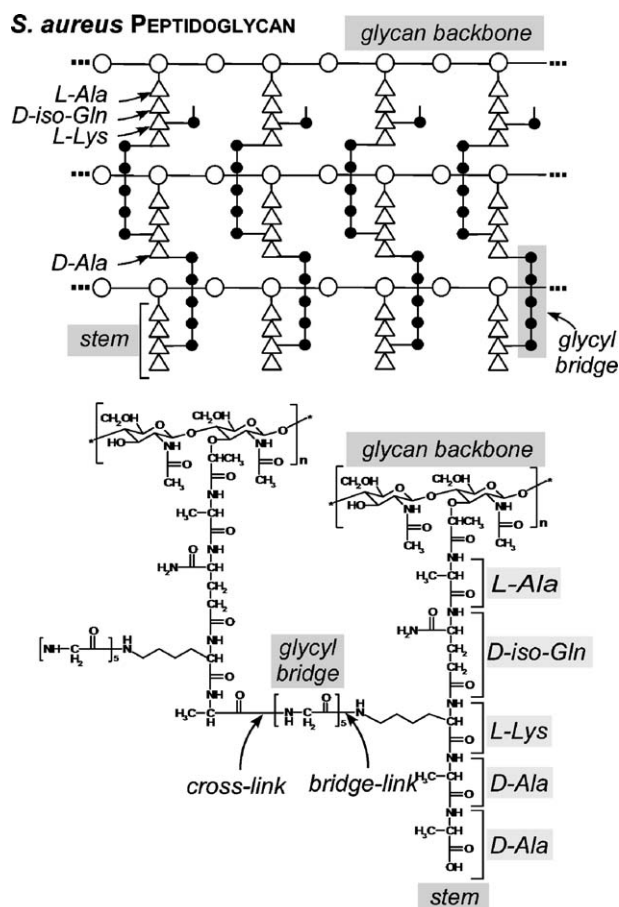
Fig. 10. (Top) Schematic representation of an idealized version of the cell-wall peptidoglycan of *S. aureus* (after Stryer). A four-unit peptide stem (triangles) having the sequence, L-Ala–D-iso-Gln–L-Lys–D-Ala, is attached to every second sugar of the glycan backbone (open circles). Cross-linking between glycans occurs through pentaglycyl bridges (dark circles) connecting the carbonyl carbon of D-Ala of the fourth position of one stem with the ε nitrogen of L-Lys of the third position of another. (Bottom) Chemical structure of the peptidoglycan of *S. aureus*. The five-residue stem on the right has no cross-link to its D-Ala–D-Ala terminus.

For many years, vancomycin was only used in the clinic as a last resort because of its toxicity and the relatively high costs associated with its administration. When used, however, it was consistently effective [93,95,96]. This began to change with the emergence of vancomycin-resistant enterococci and staphylococci. Vancomycin-resistant enterococci (VRE) appeared around 1988 [97]. The first clinical isolate of *S. aureus* with reduced susceptibility to vancomycin (minimum inhibitory concentration, MIC, equal to 8 μg/mL) was identified in Japan in 1996 [98]. Full resistance corresponds to an MIC of at least 32 μg/mL. In 2002, vancomycin-resistant *S. aureus* (VRSA) with an MIC >128 μg/mL was recovered from a patient in Michigan who was being treated with multiple courses of antibiotics [99]. Vancomycin-resistant *E. faecalis* was also recovered from the patient. The VRSA isolate contained the *vanA* vancomycin-resistance gene clusters from enterococci that code for the production of D-Ala–D-Lac stem termini and result in reduced vancomycin binding affinity. This probably occurred through conjugative transfer from the VRE isolate [100]. In

2002 and 2004, two other VRSA clinical isolates of the VanA type were documented in Pennsylvania and New York [101].

## 4.2. Potent vancomycin-like glycopeptides

Fluorophenylbenzyl-vancomycin (FPBV) is a vancomycin derivative exhibiting improved activity against VRE that have D-Ala–D-Lac stem termini. FPBV is an analog of $[^{19}F]$ oritavancin (Eli Lilly compound LY329332). Both have a hydrophobic disaccharide substituent and both show 100-fold increased activity relative to their parent compounds (Fig. 11, vertical arrows) on standard tests against VRE [96,98,99, 102,103]. Both chloroeremomycin and $[^{19}F]$oritavancin have 4-epi-vancosamine backbone substituents and both have 10-fold greater antimicrobial activity against VRE, relative to their non-substituted analogues, vancomycin and FPBV (Fig. 11, horizontal arrows). Thus, disaccharide substitution and the presence or absence of 4-epi-vancosamine appear to be important factors for the enhanced antimicrobial activity of these vancomycin-like glycopeptides. Neither factor appears to be directly associated with the D-Ala–D-Ala binding site. An understanding of where the sugars and sugar substituents are located relative to the stem termini should help in establishing modes of action for these drugs.

## 4.3. $[^{19}F]$oritavancin proximity to the pentaglycyl bridge and attached stems

We have used REDOR techniques to measure several distances from $[^{19}F]$oritavancin, Eli Lilly compound LY329332 (Fig. 11), and $^{13}C$, $^{15}N$, and $^{2}H$ labels incorporated in the cell walls of *S. aureus* [104,105]. The drug was complexed to both isolated cell walls and the cell walls of intact late log-phase whole cells. Results from the REDOR experiments demonstrated that when complexed with mature cells, $[^{19}F]$oritavancin does not form dimers. Based on $^{13}C\{^{19}F\}$ REDOR experiments on cell-wall complexes of vancomycin-susceptible *S. aureus* (Figs. 12 and 13), the $^{19}F$ of $[^{19}F]$oritavancin is near a pentaglycyl bridge connecting two stems [104]. For low occupancy, all occupied binding sites are stems ending in D-Ala–D-Ala [104]. The bridges are far enough apart that it is unlikely for two bridges to be near any single vancomycin (cf, below). Fig. 14 shows the allowed positions of the $^{19}F$ relative to the five carbonyl carbons of a compact bridge consistent with the REDOR dephasing [104]. These positions were used to calculate the dephasing shown in Fig. 13 (solid line). The fluorine can be near one end of the bridge or the other. The nearest glycyl carbonyl carbon is 5 Å from the $^{19}F$ and the farthest is 11 Å. The calculated dephasing plateau is 6%. The absence of an $^{15}N\{^{19}F\}$ REDOR difference for the amide nitrogen connecting the bridge to the stem [104] rules out placement of the fluorine at that end of the bridge (the bridge-link end). The fluorine must therefore be near the cross-link site [104].

From other REDOR experiments, we determined that the fluorine of $[^{19}F]$oritavancin is 7.4 Å from the carbonyl-carbon $^{13}C$ of the D-Ala–Gly-1 cross-link that connects the two stems, and approximately 8 Å from the carbonyl carbon of
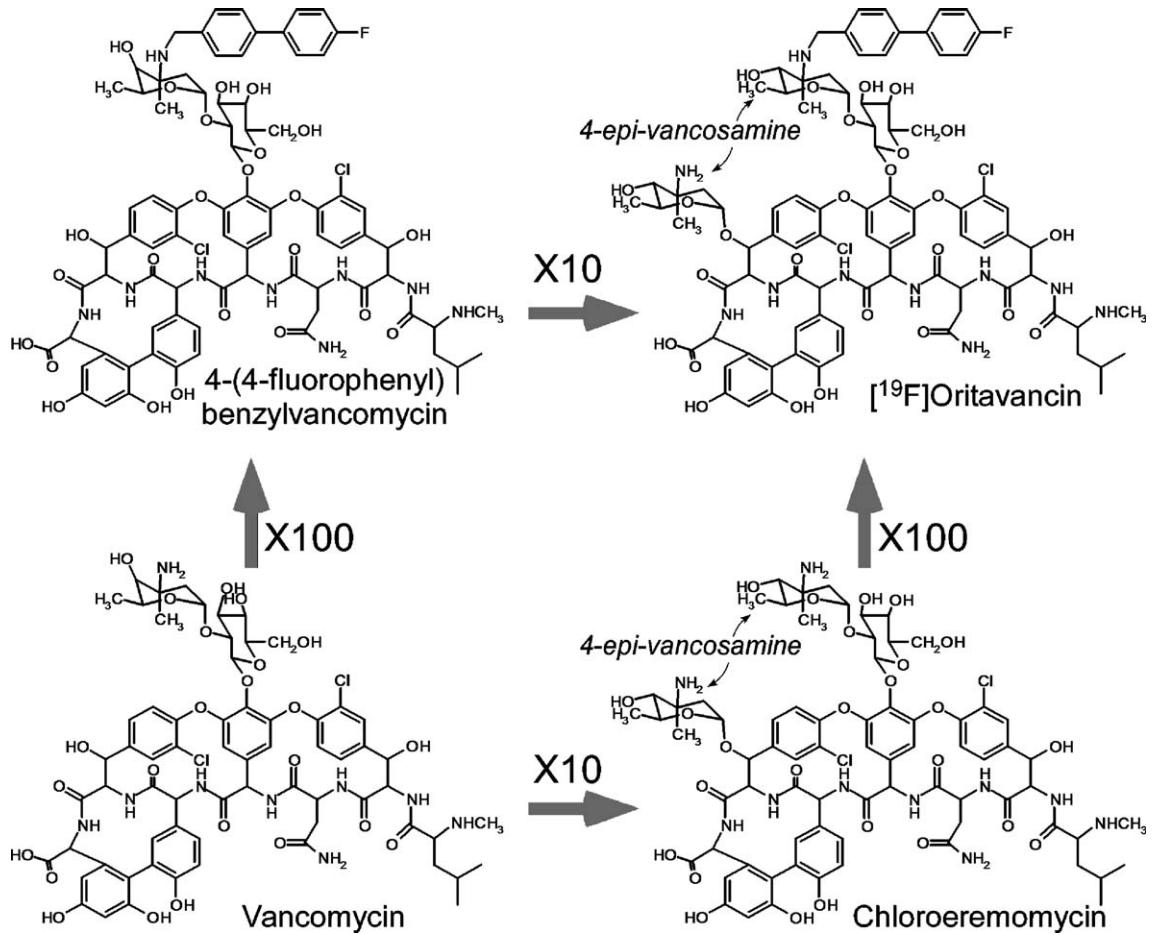
Fig. 11. Structures of vancomycin, chloroeremomycin, FPBV (upper left) and [19F]oritavancin. The arrows show the relative enhancements of glycopeptide antimicrobial activities against vancomycin-resistant enterococci (after S. J. Kim).
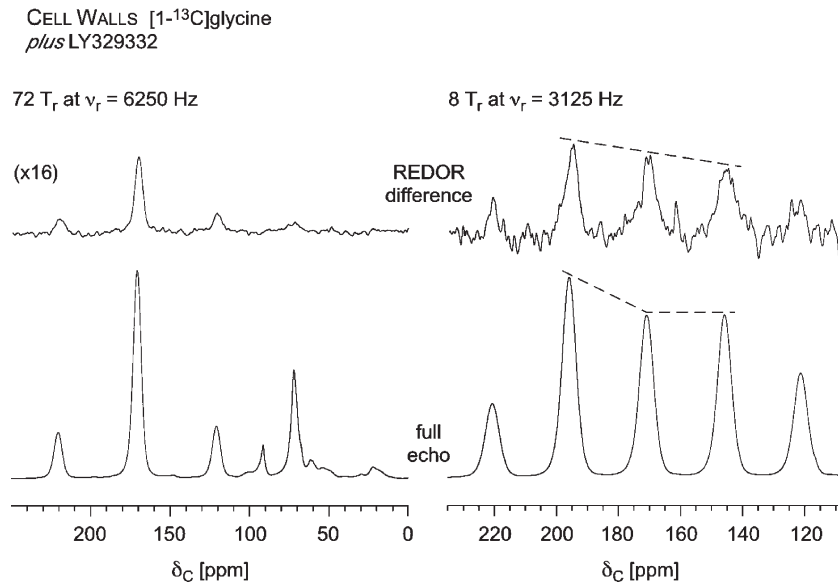


Fig. 12. $^{13}$C{$^{19}$F} REDOR NMR spectra for a complex of [19F]oritavancin (Eli Lilly compound LY329332) with cell walls of *S. aureus* grown on media containing [1-$^{13}$C]glycine [103]. REDOR differences ($\Delta S$) are shown at the top of the figure and the full echoes ($S_o$) at the bottom. $\Delta S = S_o - S$, where $S$ and $S_o$ are the signal intensities with and without $^{19}$F dephasing pulses, respectively. Expanded frequency-scale plots of the carbonyl-carbon regions of the REDOR spectra after 8 rotor cycles of dipolar evolution (only the signal of the labeled carbonyl-carbon nearest to $^{19}$F is dephased) are shown to the right of the figure. The dissimilarity of the REDOR difference and full-echo spectra (dotted lines) indicates an orientational preference for the $^{13}$C–$^{19}$F internuclear vector relative to the $^{13}$C carbonyl-carbon chemical shift tensor.
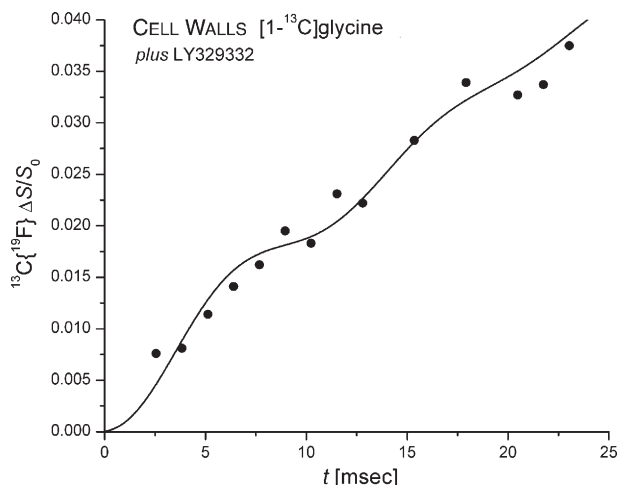
Fig. 13. $^{13}$C{$^{19}$F} REDOR dephasing ($\Delta S/S_o$) as a function of the dipolar evolution time, t, for a complex of [$^{19}$F]oritavancin with cell walls (circles) of *S. aureus* grown on media containing [1-$^{13}$C]glycine [104]. The binding-site occupancy for 2 μmol of the antibiotic complexed to the cell walls was 16%. The solid line shows the calculated dephasing assuming the $^{13}$C–$^{19}$F distances of the model shown in Fig. 15. The breaks in the calculated dephasing arise from the presence of five significantly different $^{13}$C–$^{19}$F dipolar couplings.

L-Ala of the neighboring stem, with the α carbon closer than the carbonyl carbon and the methyl carbon farther [105].

### 4.4. Model of the [$^{19}$F]oritavancin binding site

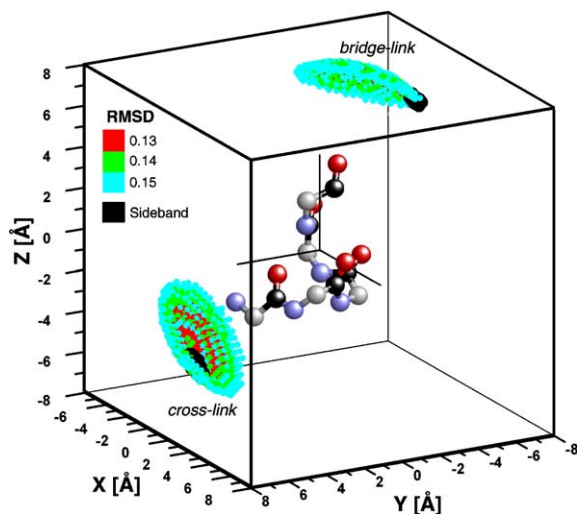A cartoon model of the binding site consistent with the REDOR results, binding-assay results, and cell-wall composi-



Fig. 14. Possible positions for the $^{19}$F of [$^{19}$F]oritavancin [104] (small dots) relative to the pentaglycyl helix (carbonyl carbons in black, $C_\alpha$ in gray, nitrogens in blue, and oxygens in red) consistent with the REDOR dephasing of Figs. 12 and 13. The colors of the $^{19}$F positions indicate the RMSD between calculated and experimental dephasing. The best match shown (red) has a 13% error and the worst match (blue) a 15% error. Most likely placements of $^{19}$F relative to the end carbonyl carbons determined by analysis of the spinning sideband intensities of Fig. 12 (right) are shown in black. The bridge-link site is near the top cluster and the cross-link site near the bottom cluster. The absence of an $^{15}$N{$^{19}$F} REDOR difference for the amide nitrogen connecting the bridge to the stem (see Fig. 15, left) rules out placement of the $^{19}$F near the bridge-link.

tional analysis is shown in Fig. 15. The model assumes that the aglycon cleft binds to a stem terminating in D-Ala–D-Ala in a locally ordered peptidoglycan matrix. This sort of termination is indicated by a ball at the bottom of the stem. The cross-link is attached offset from the idealized stem cylinder (for example, see the cross-link at center, left). The peptidoglycan of *S. aureus* has about ten layers of glycans, only two of which are shown in Fig. 15. In addition, the glycan chains in both layers are shown for clarity as strictly parallel, which need not be the case; chains in adjacent layers may be oblique or rotated about their long axes relative to one another. In the model, the fluorine of the biphenyl moiety is not near the L-Ala of the complexed stem, but rather the L-Ala of a nearest-neighbor stem on an adjacent glycan strand. This nearest-neighbor stem is shown with a bridge (85% of all stems have a bridge), and this arrangement is the source of $^{19}$F coupling to the carbonyl carbons of Gly as well as D-Ala. The complex is presumably stabilized by interactions of the sugars of [$^{19}$F]oritavancin with peptidoglycan sugars. One of these possible interactions is shown in the center foreground; the other is obscured by the cross-link of the complexed stem in the foreground [104]. This stabilization may help to explain the potency of [$^{19}$F]oritavancin against VRE with D-Ala–D-Lac stem termini. A space-filling rendering of the aglycon binding site, the bound stem, the neighboring stem, and the cross-linking bridge connecting the two is shown in Fig. 16.

### 4.5. Complexes at the membrane surface

We enhanced the fraction of observed complexes that are at the membrane surface by adding glycopeptide and labels for
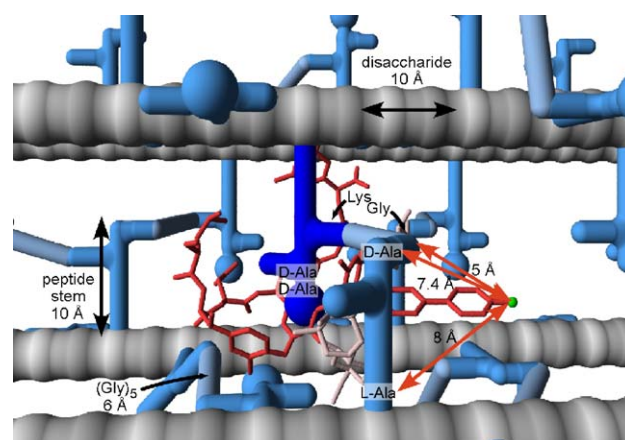


Fig. 15. Molecular model of the binding of [$^{19}$F]oritavancin in mature peptidoglycan of *S. aureus* [104]. The glycan strands are shown as gray cylinders, the peptide stems as blue cylinders, and the pentaglycyl bridges as light blue cylinders. The helical pitch of the glycan chain places adjacent stems on the same chain at right angles to one another. Stems ending in D-Ala–D-Ala have a ball at the end. The vancomycin cleft is shown attached to a stem (dark blue) ending in D-Ala–D-Ala. The sugar sidechains of [$^{19}$F]oritavancin are shown in white and the $^{19}$F label in green. The $^{19}$F is 8 Å from the carbonyl carbon of the L-Ala at the base of the peptide stem in the center foreground, 7.4 Å from the carbonyl carbon of D-Ala at the tip of this stem, and 5 Å from the carbonyl carbon of Gly$_5$ of the pentaglycyl bridge cross-linked to this stem. Other experimentally established distances are in black.
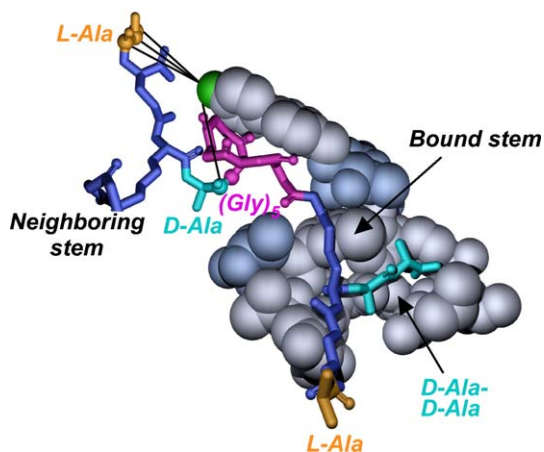
Fig. 16. Space-filling model of [$^{19}$F]oritavancin with sugars shown in light blue, and the aglycon and biphenyl in gray. The D-Ala–D-Ala terminus of a stem bound to the oritavancin is shown in blue-green, and the cross-linking bridge to a neighboring stem is shown in red. Both stems are blue. The distance from the fluorine (green) to the D-Ala carbonyl carbon of the cross-link site is 7.4 Å (solid line), and to the three carbons of L-Ala of the neighboring stem, about 8 Å (solid lines). The location of the L-Lys sidechain of the neighboring stem is not defined.

stems and bridges to rapidly dividing cells [106]. We harvested whole cells in less than one doubling time for solids NMR analysis. This is the same protocol used to characterize biosynthesis [94], only now the goal was to characterize bound structures using a variety of labeling schemes. For whole cells of vancomycin-susceptible *S. aureus* grown in the presence of [1-$^{13}$C]glycine and L-[ε-$^{15}$N]lysine, contact between an [ε-$^{15}$N]lysyl amide bridge-link and [$^{19}$F]oritavancin was observed for exponentially growing cells [106] but not for mature cells [104,106]. Although some of the [$^{19}$F]oritavancin was bound to partially cross-linked, mature peptidoglycan as before, with $^{19}$F proximate to the cross-link site but not the bridge-link site (Fig. 14), a sizeable fraction of the [$^{19}$F] oritavancin must be bound to D-Ala–D-Ala termini of stems at or near the membrane surface. The observed new $^{15}$N–$^{19}$F contact is therefore to the stems of growing new strands that are neighboring bound stems. The proximity of the fluorobiphenyl apparently interferes with the formation of the cross-link between a bound stem and its neighboring stem (Fig. 16), and forces a relocation of the bridge and bridge-link site of the neighboring stem so that $^{15}$N{$^{19}$F} dephasing is now observed [106]. This result suggests an interference with transpeptidation. At the same time, the observed increase in peptidoglycan precursors and decrease in the number of stems with bridges [106] suggests an interference with transglycosylation [94]. Thus, the mode of action of oritavancin acting on vancomycin-susceptible *S. aureus* is mixed [106].

## 5. Conclusions

The constant challenge to combat human infectious diseases requires knowledge of the structural interactions between pathogen and host. Atomic-level details to help define the modes of action of antibiotics are vital for speeding up the difficult task of discovering new antibiotics and overcoming the too-rapid emergence of antibiotic resistance.

We have shown the applications of REDOR, a solid-state NMR technique under magic angle spinning (high resolution) conditions, for two highly potent peptide antibiotics. For K3, a synthetic analogue of a magainin-like antimicrobial peptide, REDOR, in conjunction with static NMR experiments on oriented samples, revealed a torus-type pore formation in the bilayers of DPPC-DPPG, in which K3 monomers, dimers and phospholipid headgroups together line the wall of the pore. For oritavancin, a vancomycin-analogue, intermolecular distance and orientation restraints from REDOR suggested an interference with both transglycosylation and transpeptidation in the cell walls of *S. aureus*. The mixed mode of action of oritavancin might be responsible for its increased activity against VRE.

The REDOR strategy is generally not one of total structure determination, but rather one of accessing site-specific atomic-level information to yield parameters characterizing structure, dynamics, and metabolism in large, heterogeneous systems. REDOR therefore complements other MAS [2,107–113] and static NMR experiments [1,84] in providing useful tools for structural biologists in answering specific questions regarding the structure and function of membrane proteins and poorly soluble biomolecular complexes generally.

## References

[1] B. Bechinger, The structure, dynamics and orientation of antimicrobial peptides in membranes by multidimensional solid-state NMR spectroscopy, Biochim. Biophys. Acta 1462 (1999) 157–183.

[2] D. Huster, Investigations of the structure and dynamics of membrane-associated peptides by magic angle spinning NMR, Prog. Nucl. Magn. Reson. Spectrosc. 46 (2005) 79–107.

[3] T. Gullion, J. Schaefer, Rotational echo double-resonance NMR, J. Magn. Res. 81 (1989) 196–200.

[4] T. Gullion, J. Schaefer, Detection of weak heteronuclear dipolar coupling by rotational echo double-resonance, Adv. Magn. Res. 13 (1989) 57–83.

[5] Y. Pan, T. Gullion, J. Schaefer, Determination of C–N internuclear distances by rotational-echo double-resonance NMR of solids, J. Magn. Res. 90 (1990) 330–340.

[6] W.L. Maloy, U.P. Kari, Structure–activity studies on magainins and other host defense peptides, Biopolymers 37 (1995) 105–122.

[7] E. Soravia, G. Martini, M. Zasloff, Antimicrobial properties of peptides from *Xenopus* granular gland secretions, FEBS Lett. 228 (1988) 337–340.

[8] M. Zasloff, Magainins, a class of antimicrobial peptides from *Xenopus* skin: isolation, characterization of two active forms, and partial cDNA sequence of a precursor, Proc. Natl. Acad. Sci. U. S. A. 84 (1987) 5449–5453.

[9] K. Matsuzaki, Magainins as paradigm for the mode of action of pore forming polypeptides, Biochim. Biophys. Acta 1376 (1998) 391–400.

[10] H.W. Huang, Action of antimicrobial peptides: two-state model, Biochemistry 39 (2000) 8347–8352.

[11] M. Mehring, Principles of High Resolution NMR in Solids, 2nd edn. Springer-Verlag, Berlin, 1983.

[12] C.P. Slichter, Principles of Magnetic Resonance, 3rd edn.Springer-Verlag, Berlin, 1990.

[13] K. Schmidt-Rohr, H.W. Spiess, Multidimensional Solid-State NMR and Polymers, Academic Press, 1997.

[14] E.O. Stejskal, J.D. Memory, High Resolution NMR in the Solid State, Oxford Univ. Press, New York, 1994.

[15] R.S. Prosser, S.A. Hunt, R.R. Vold, Improving sensitivity in mechanically oriented phospholipid bilayers using ultrathin glass plates — a deuterium solid state NMR study, J. Magn. Res., B 109 (1996) 109–111.

[16] J. Torbet, Using magnetic orientation to study structure and assembly, Trends Biochem. Sci. 12 (1987) 327–330.

[17] C.R. Sanders, B.J. Hare, K. Howard, J.H. Prestegard, Magnetically-oriented phospholipid micelles as a tool for the study of membrane-associated molecules, Progr. NMR Spectr. 26 (1993) 421–444.

[18] M. Lee, W.I. Goldburg, Nuclear-magnetic-resonance line narrowing by a rotating magnetic field, Phys. Rev., A 140 (1965) 1261–1271.

[19] P. Mansfield, D. Ware, Nuclear resonance line narrowing in solids by repeated short pulse r.f. irradiation, Phys. Lett. 22 (1966) 133–135.

[20] E.D. Ostroff, J.S. Waugh, Multiple spin echoes and spin locking in solids, Phys. Rev. Lett. 16 (1966) 1097–1098.

[21] J.S. Waugh, Uncoupling of local field spectra in nuclear magnetic resonance: determination of atomic positions in solids, Proc. Natl. Acad. Sci. U. S. A. 73 (1976) 1394–1397.

[22] R.K. Hester, J.L. Ackerman, B.L. Neff, J.S. Waugh, Separated local field spectra in NMR: determination of structure of solids, Phys. Rev. Lett. 36 (1976) 1081–1083.

[23] C.H. Wu, A. Ramamoorthy, S.J. Opella, High-resolution heteronuclear dipolar solid-state NMR spectroscopy, J. Magn. Reson., A 109 (1994) 270–272.

[24] E.R. Andrew, A. Bradbury, R.G. Eades, Nuclear magnetic resonance spectra from a crystal rotated at high speed, Nature 182 (1958) 1659.

[25] I.J. Lowe, Free induction decays of rotating solids, Phys. Rev. Lett. 2 (1959) 285–287.

[26] A.E. Bennett, R.G. Griffin, S. Vega, Recoupling of homo- and heteronuclear dipolar interactions in rotating solids, in: P. Diehl, E. Fluck, H. Gunther, R. Kosfeld, J. Seelig (Eds.), NMR Basic Principles and Progress, vol. 33, Springer-Verlag, Berlin Heidelberg, 1994, pp. 1–77.

[27] R.G. Griffin, Dipolar recoupling in MAS spectra of biological solids, Nat. Struct. Biol. 5 (1998) 508–512 (Suppl.).

[28] S. Dusold, A. Sebald, Dipolar recoupling under magic-angle spinning conditions, Ann. Rep. NMR Spectr. 41 (2000) 185–264.

[29] T. Gullion, D.B. Baker, M.S. Conradi, New, compensated Carr–Purcell Sequences, J. Magn. Reson. 89 (1990) 479–484.

[30] A.W. Hing, S. Vega, J. Schaefer, Transferred-echo double-resonance NMR, J. Magn. Res. 96 (1992) 205–209.

[31] D.P. Raleigh, M.H. Levitt, R.G. Griffin, Rotational resonance in solid state NMR, Chem. Phys. Lett. 146 (1988) 71–76.

[32] R. Tycko, G. Dabbagh, Measurement of nuclear magnetic dipole–dipole couplings in magic angle spinning NMR, Chem. Phys. Lett. 173 (1990) 461–465.

[33] T. Gullion, S. Vega, A simple magic angle spinning NMR experiment for the dephasing of rotational echoes of dipolar coupled homonuclear spin pairs, Chem. Phys. Lett. 194 (1992) 423–428.

[34] W. Zhu, C.A. Klug, J. Schaefer, Measurement of dipolar coupling within isolated spin-1/2 homonuclear pairs by CEDRA NMR, J. Magn. Reson. 108 (1994) 121–123.

[35] D.M. Gregory, D.J. Mitchell, J.A. Stringer, S. Kiihne, J.C. Shiels, J. Callahan, M.A. Mehta, G.P. Drobny, Windowless dipolar recoupling: the detection of weak dipolar couplings between spin 1/2 nuclei with large chemical shift anisotropies, Chem. Phys. Lett. 246 (1995) 654–663.

[36] J.M. Joers, R. Rosanske, T. Gullion, J.R. Garbow, Detection of dipolar interactions by CROWN NMR, J. Magn. Reson., A 106 (1994) 123–126.

[37] N.C. Nielsen, H. Bildsoe, H.J. Jakobsen, M.H. Levitt, Double-quantum homonuclear rotary resonance-efficient dipolar recovery in magic-angle-spinning, J. Chem. Phys. 101 (1994) 1805–1812.

[38] W. Sommer, J. Gottwald, D.E. Demco, H.W. Spiess, Dipolar heteronuclear multiple-quantum NMR-spectroscopy in rotating solids, J. Magn. Reson., A 113 (1995) 131–134.

[39] Y.K. Lee, N.D. Kurur, M. Helmle, O.G. Johannessen, N.C. Nielsen, M.H. Levitt, Efficient dipolar recoupling in the NMR of rotating solids — a sevenfold symmetrical radiofrequency pulse sequence, Chem. Phys. Lett. 242 (1995) 304–309.

[40] A.E. Bennett, J.H. Ok, R.G. Griffin, S. Vega, Chemical-shift correlation spectroscopy in rotating solids-radio frequency-driven dipolar recoupling and longitudinal exchange, J. Chem. Phys. 96 (1992) 8624–8627.

[41] B.-Q. Sun, P.R. Costa, D. Kosisko, P.T. Lansbury Jr., R.G. Griffin, Internuclear distance measurements in solid-state nuclear-magnetic-resonance–Dipolar recoupling via rotor synchronized spin locking, J. Chem. Phys. 102 (1995) 702–707.

[42] M.H. Levitt, T.G. Oas, R.G. Griffin, Rotary resonance recoupling in heteronuclear spin pair systems, Isr. J. Chem. 28 (1988) 271–282.

[43] T.G. Oas, M.H. Levitt, R.G. Griffin, Rotary resonance recoupling of dipolar interactions in solid-state nuclear magnetic-resonance spectroscopy, J. Chem. Phys. 89 (1988) 692–695.

[44] M.H. Levitt, Symmetry-based pulse sequences in magic-angle spinning solid-state NMR, in: D.M. Grant, R.K. Harris (Eds.), Encyclopedia of Nuclear Magnetic Resonance: Supplementary Volume, Wiley, Chichester, England, 2002, pp. 165–196.

[45] P. Nicolas, A. Mor, Peptides as weapons against microorganisms in the chemical defense system of vertebrates, Annu. Rev. Microbiol. 49 (1995) 277–304.

[46] R.M. Ep, H.J. Vogel, Diversity of antimicrobial peptides and their mechanisms of action, Biochim. Biophys. Acta 1462 (1999) 11–28.

[47] W. Van't Hof, E.C.I. Veerman, E.J. Helmerhorst, A.V.N. Amerongenm, Antimicrobial peptides: properties and applicability, Biol. Chem. 382 (2001) 597–619.

[48] A. Tossi, L. Sandri, A. Giangaspero, Amphipathic, alpha-helical antimicrobial peptides, Biopolymers 55 (2000) 4–30.

[49] R.E.W. Hancock, G. Diamond, The role of cationic antimicrobial peptides in innate host defenses, Trends Microbiol. 8 (2000) 402–410.

[50] Y. Shai, Mode of action of membrane active antimicrobial peptides, Biopolymers 66 (2002) 236–248.

[51] O. Toke, Antimicrobial peptides: new candidates in the fight against bacterial infections, Biopolymers 80 (2005) 717–735.

[52] M. Wu, E. Maier, R. Benz, R.E.W. Hancock, Mechanism of interaction of different classes of cationic antimicrobial peptides with planar bilayers and with the cytoplasmic membrane of *Escherichia coli*, Biochemistry 38 (1999) 7235–7242.

[53] M.L. Mangoni, N. Papo, D. Barra, M. Simmaco, A. Bozzi, A. Di Giulio, A.C. Rinaldi, Effects of the antimicrobial peptide temporin L on cell morphology, membrane permeability and viability of *Escherichia coli*, Biochem. J. 380 (2004) 859–865.

[54] G. Ehrenstein, H. Lecar, Electrically gated ionic channels in lipid bilayers, Q. Rev. Biophys 10 (1977) 1–34.

[55] D.M. Ojcius, J.D. Young, Cytolytic pore-forming proteins and peptides: is there a common structural motif? Trends Biochem. Sci. 16 (1991) 225–229.

[56] Y. Pouny, D. Rapaport, A. Mor, P. Nicolas, Y. Shai, Interaction of antimicrobial dermaseptin and its fluorescently labeled analogues with phospholipid membranes, Biochemistry 31 (1992) 12416–12423.

[57] Y. Shai, Molecular recognition between membrane-spanning polypeptides, Trends Biochem. Sci. 20 (1995) 460–464.

[58] Y. Shai, Mechanism of the binding, insertion and destabilization of phospholipid bilayer membranes by alpha-helical antimicrobial and cell non-selective membrane-lytic peptides, Biochim. Biophys. Acta 1462 (1999) 55–70.

[59] S.J. Ludtke, K. He, W.T. Heller, T.A. Harroun, L. Yang, H.W. Huang, Membrane pores induced by magainin, Biochemistry 35 (1996) 13723–13728.

[60] Y.Q. Tang, J. Yuan, G. Osapay, K. Osapay, D. Tran, C.J. Miller, A.J. Ouellette, M.E. Selsted, A cyclic antimicrobial peptide produced in primate leukocytes by the ligation of two truncated alpha-defensins, Science 286 (1999) 498–502.

[61] J.J. Buffy, M.J. McCormick, S. Wi, A. Waring, R.I. Lehrer, M. Hong, Solid-state NMR investigation of the selective perturbation of lipid bilayers by the cyclic antimicrobial peptide RTD-1, Biochemistry 43 (2004) 9800–9812.

[62] D.S. Wishart, B.D. Sykes, F.M. Richards, The chemical shift index: a fast and simple method for the assignment of protein secondary structure through NMR spectroscopy, Biochemistry 31 (1992) 1647–1651.

[63] D.S. Wishart, B.D. Sykes, The $^{13}$C chemical-shift index: a simple method for the identification of protein secondary structure using $^{13}$C chemical-shift data, J. Biomol. NMR 4 (1994) 171–180.

[64] G. Cornilescu, F. Delaglio, A. Bax, Protein backbone angle restraints from searching a database for chemical shift and sequence homology, J. Biomol. NMR 13 (1999) 289–302.

[65] A.C. deDios, J.G. Pearson, E. Oldfield, Secondary and tertiary structural effects on protein NMR chemical shifts: an ab initio approach, Science 260 (1993) 1491–1496.

[66] E. Oldfield, Chemical shifts in amino acids, peptides, and proteins: from quantum chemistry to drug design, Annu. Rev. Phys. Chem. 53 (2002) 349–378.

[67] H. Sun, L.K. Sanders, E. Oldfield, Carbon-13 NMR shielding in the twenty common amino acids: comparisons with experimental results in proteins, J. Am. Chem. Soc. 124 (2002) 5486–5495.

[68] J. Birn, A. Poon, Y. Mao, A. Ramamoorthy, Ab initio study of (13)C (alpha) chemical shift anisotropy tensors in peptides, J. Am. Chem. Soc. 126 (2004) 8529–8534.

[69] H. Saito, Conformation-dependent $^{13}$C chemical shifts: a new means of conformational characterization as obtained by high-resolution solid-state $^{13}$C NMR, Magn. Res. Chem. 24 (1986) 835–852.

[70] O. Toke, W.L. Maloy, S.J. Kim, J. Blazyk, J. Schaefer, Secondary structure and lipid contact of a peptide antibiotic in phospholipid bilayers by REDOR, Biophys. J. 87 (2004) 662–674.

[71] F. Porcelli, B. Buck, D.K. Lee, K.J. Hallock, A. Ramamoorthy, G. Veglia, Structure and orientation of pardaxin determined by NMR experiments in model membranes, J. Biol. Chem. 279 (2004) 45815–45823.

[72] D.J. Hirsh, J. Hammer, W.L. Maloy, J. Blazyk, J. Schaefer, Secondary structure and location of a magainin analogue in synthetic phospholipid bilayers, Biochemistry 35 (1996) 12733–12741.

[73] O. Toke, R.D. O'Connor, T.K. Weldeghiorghis, W.L. Maloy, R.W. Glaser, A.S. Ulrich, J. Schaefer, Structure of (KIAGKIA)$_3$ aggregates in phospholipid bilayers by solid-state NMR, Biophys. J. 87 (2004) 675–687.

[74] K. Matsuzaki, O. Murase, H. Tokuda, S. Funakoshi, N. Fujii, K. Miyajima, Orientational and aggregational states of magainin 2 in phospholipid bilayers, Biochemistry 33 (1994) 3342–3349.

[75] K. Matsuzaki, Y. Mitani, K. Akada, O. Murase, S. Yoneyama, M. Zasloff, K. Miyajima, Mechanism of synergism between antimicrobial peptides magainin 2 and PGLa, Biochemistry 37 (1998) 15144–15153.

[76] R.D. O'Connor, J. Schaefer, Relative CSA-dipolar orientation from REDOR sidebands, J. Magn. Res. 154 (2002) 46–52.

[77] D.J. Gordon, J.J. Balbach, R. Tycko, S.C. Meredith, Increasing the amphiphilicity of an amyloidogenic peptide changes the beta-sheet structure in the fibrils from antiparallel to parallel, Biophys. J. 86 (2004) 428–434.

[78] N.A. Oyler, R. Tycko, Absolute structural constraints on amyloid fibrils from solid-state NMR spectroscopy of partially oriented samples, J. Am. Chem. Soc. 126 (2004) 4478–4479.

[79] K.L. Wooley, C.A. Klug, K. Tasaki, J. Schaefer, Shapes of dendrimers from rotational-echo double resonance NMR, J. Am. Chem. Soc. 119 (1997) 53–58.

[80] B. Bechinger, M. Zasloff, S.J. Opella, Structure and orientation of the antibiotic peptide magainin in membranes by solid-state nuclear magnetic resonance spectroscopy, Prot. Sci. 2 (1993) 2077–2084.

[81] S. Yamaguchi, T. Hong, A. Waring, R.I. Lehrer, M. Hong, Solid-state NMR investigations of peptide–lipid interaction and orientation of a beta-sheet antimicrobial peptide, protegrin, Biochemistry 41 (2002) 9852–9862.

[82] K.A. Henzler Wildman, D.K. Lee, A. Ramamoorthy, Mechanism of lipid bilayer disruption by the human antimicrobial peptide, LL-37, Biochemistry 42 (2003) 6545–6558.

[83] R.W. Glaser, C. Sachse, U.H. Durr, P. Wadhwani, S. Afonin, E. Strandberg, A.S. Ulrich, Concentration-dependent realignment of the antimicrobial peptide PGLa in lipid membranes observed by solid-state 19F-NMR, Biophys. J. 88 (2005) 3392–3397.

[84] S.J. Opella, F.M. Marassi, Structure determination of membrane proteins by NMR spectroscopy, Chem. Rev. 104 (2004) 3587–3606.

[85] I.C.P. Smith, I.H. Eikel, Phosphorous-31 NMR of phospholipids in membranes, Phosphorous-31 NMR Principles and Applications, Academic Press, Inc., 1984.

[86] Y. Shai, Mode of action of membrane active antimicrobial peptides, Biopolymers 66 (2002) 236–248.

[87] P.E. Reynolds, E.A. Somner, Comparison of the target sites and mechanisms of action of glycopeptide and lipoglycodepsipeptide antibiotics, Drug. Exp. Clin. Res. 16 (1990) 385–389.

[88] E. Molitor, C. Kluczny, H. Brotz, G. Bierbaum, R. Jack, H.G. Sahl, Effects of the lantibiotic mersacidin on the morphology of staphylococci, Zentralbl. Bakteriol. 284 (1996) 318–328.

[89] J.C. Barna, D.H. Williams, The structure and mode of action of glycopeptide antibiotics of the vancomycin group, Annu. Rev. Microbiol. 38 (1984) 339–357.

[90] H.R. Perkins, Specificity of combination between mucopeptide precursors and vancomycin or ristocetin, Biochem J. 111 (1969) 195–205.

[91] J.S. Anderson, M. Matsuhashi, M.A. Haskin, J.L. Strominger, Biosynthesis of the peptidoglycan of bacterial cell walls: II. Phospholipid carriers in the reaction sequence, J. Biol. Chem. 242 (1967) 3180–3190.

[92] H. Brotz, G. Bierbaum, P.E. Reynolds, H.G. Sahl, The lantibiotic mersacidin inhibits peptidoglycan biosynthesis at the level of transglycosylation, Eur. J. Biochem. 246 (1997) 193–199.

[93] P.E. Reynolds, Structure, biochemistry and mechanism of action of glycopeptide antibiotics, Eur. J. Clin. Microbiol. 8 (1989) 943–950.

[94] L. Cegelski, S.J. Kim, A.W. Hing, D.R. Studelska, R.D. O'Connor, A.K. Mehta, J. Schaefer, Rotational-echo double resonance characterization of the effects of vancomycin on cell wall synthesis in Staphylococcus aureus, Biochemistry 41 (2002) 13053–13058.

[95] F.L. Sapico, J.Z. Montgomerie, H.N. Canawati, G. Aeilts, Methicillin-resistant Staphylococcus aureus bacteriuria, Am. J. Med. Sci. 281 (1981) 101–109.

[96] K. Sieradzki, A. Tomasz, A highly vancomycin-resistant laboratory mutant of Staphylococcus aureus, FEMS Microbial. Lett. 142 (1996) 161–166.

[97] A.P. Johnson, A.H. Uttley, N. Woodford, R.C. George, Resistance to vancomycin and teicoplanin: an emerging clinical problem, Clin. Microbiol. Rev. 3 (1990) 280–291.

[98] K. Hiramatsu, N. Aritaka, H. Hanaki, S. Kawasaki, Y. Hosoda, S. Hori, Y. Fukuchi, I. Kobayashi, Dissemination in Japanese hospitals of strains of Staphylococcus aureus heterogeneously resistant to vancomycin, Lancet 350 (1997) 1670–1673.

[99] CDC, Staphylococcus aureus resistant to vancomycin—United States, Morb. Mortal. Wkly. Rep. 51 (2002) 565–567.

[100] W.C. Noble, Z. Virani, R.G. Cree, Co-transfer of vancomycin and other resistance genes from Enterococcus faecalis NCTC 12201 to Staphylococcus aureus, FEMS Microbial. Lett. 72 (1992) 195–198.

[101] CDC, Vancomycin-resistant Staphylococcus aureus — Pennsylvania, Morb. Mortal. Wkly. Rep. 51 (2002) 902.

[102] S.J. Projan, Why is big Pharma getting out of antibacterial drug discovery? Curr. Opin. Microbiol. 6 (2003) 427–430.

[103] A.P. Johnson, A.H. Uttley, N. Woodford, R.C. George, Resistance to vancomycin and teicoplanin: an emerging clinical problem, Clin. Microbiol. Rev. 3 (1990) 280–291.

[104] S.J. Kim, L. Cegelski, D.R. Studelska, R.D. O'Connor, A.K. Mehta, J. Schaefer, Rotational-echo double resonance characterization of vancomycin binding sites in Staphylococcus aureus, Biochemistry 41 (2002) 6967–6977.

[105] A.K. Mehta, L. Cegelski, R.D. O'Connor, J. Schaefer, REDOR with a relative full-echo reference, J. Magn. Reson. 163 (2003) 182–187.

[106] L. Cegelski, D. Stueber, S.J. Kim, J. Schaefer, Oritavancin mode of action in Staphylococcus aureus by REDOR (in preparation).

[107] J.J. Buffy, T. Hong, S. Yamaguchi, A.J. Waring, R.I. Lehrer, M. Hong, Solid-state NMR investigation of the depth of insertion of protegrin-1

in lipid bilayers using paramagnetic $Mn^{2+}$, Biophys. J. 85 (2003) 2363–2373.

[108] J.J. Buffy, A.J. Waring, M. Hong, Determination of peptide oligomerization in lipid bilayers using $^{19}$F spin diffusion NMR, J. Am. Chem. Soc. 127 (2005) 4477–4483.

[109] M. Hong, J.D. Gross, C.M. Rienstra, R.G. Griffin, K.K. Kumashiro, K. Schmidt-Rohr, Coupling amplification in 2D MAS NMR and its application to torsion angle determination in peptides, J. Magn. Res. 129 (1997) 85–92.

[110] C.M. Rienstra, M. Hohway, L.J. Mueller, C.P. Jaroniec, B. Reif, R.G. Griffin, Determination of multiple torsion-angle constraints in U–$^{13}$C, $^{15}$N-labeled peptides: 3D $^{1}$H–$^{15}$N–$^{13}$C–$^{1}$H dipolar chemical shift NMR spectroscopy in rotating solids, J. Am. Chem. Soc. 124 (2002) 11908–11922.

[111] Y. Ishii, T. Terao, M. Kainosho, Relayed anisotropy correlation NMR: determination of dihedral angles in solids, Chem. Phys. Lett. 256 (1996) 133–144.

[112] J.C. Chan, R. Tycko, Solid-state NMR spectroscopy method for determination of the backbone torsion angle psi in peptides with isolated uniformly labelled residues, J. Am. Chem. Soc. 125 (2003) 11828–11829.

[113] M. Baldus, Correlation experiments for assignment and structure elucidation of immobilized polypeptides under magic angle spinning, Prog. Nucl. Magn. Reson. Spectrosc. 41 (2002) 1–47.